Analysis of pulsed drainage in a Hele-Shaw cell

Sascha Hilgenfeldt, Stephan A. Koehler, and Howard A. Stone
Pierce Hall, Division of Engineering and Applied Sciences
Harvard University, Cambridge MA, USA

May 2000

Abstract

Foam drainage is the flow of liquid through the network of interstitial spaces between the bubbles of a foam. The source of dissipation in the flow depends on the type of surfactant, with *node-dominated* and *channel-dominated* foam drainage as limiting cases. Numerous studies have compared the results of these theories to foam drainage in essentially one-dimensional flow geometries. We show some experimental results of the dynamics of a liquid pulse in *two dimensions* of a foam confined to a vertical Hele-Shaw cell and proceed to analyze the dynamics. In this case, an exact similarity solution to a generalized foam drainage equation in 2-D can be found. Analytical results for the movement of the pulse peak are available for arbitrary characteristic exponent of foam permeability. We review key results for the node-dominated model and compare them to the predictions of channel-dominated drainage and the best-fit hybrid model interpolating between the two drainage limits.

1 Introduction

Aqueous foams consist of bubbles which are separated by liquid and are stabilized by surfactants [1–3]. In sufficiently dry foams, the bubbles are polyhedral and the amount of liquid in the *films* between the bubbles' faces is negligible. Thus, almost all of the liquid resides in the *channels* (or *Plateau borders*), which are the regions between three touching bubbles, and in *nodes* (or *vertices*), which are the junctions of four channels. The channels and nodes form a continuous interconnected network through which liquid flows.

In the study of foam drainage it is convenient to work with the *liquid volume fraction* ϵ, which is a macroscopic quantity (i.e., defined on length scales larger than the size of a single bubble), denoting the ratio of liquid volume to total foam volume. It varies spatially and temporally as liquid flows through the channels and nodes. In the limit of small volume fractions ($\epsilon \lesssim 0.05$), the channels are long and slender with a characteristic radius of curvature r. For a Kelvin foam composed of tetrakaidecahedral bubbles (see [4, 5]) with edge length (i.e. channel length) L and volume $2^{7/2}L^3$,

$$\epsilon \approx \delta_\epsilon \left(\frac{r}{L}\right)^2 \quad \text{with } \delta_\epsilon = 12(\sqrt{3} - \pi/2)2^{-7/2} \approx 0.171\,. \tag{1}$$

Although Kelvin cells are rarely observed in nature, they provide geometric constants which are very close to those of realistic random foam cells. Foam drainage [6, 7] is the macroscopic rearrangement of the liquid phase of a foam. Drainage is driven by gravity and capillarity while viscous effects accompanying flow resist the fluid motion. Since the Reynolds numbers are generally small, it is possible to arrive at a macroscopic description of the flow analogous to porous media models. In [8] we propose that foams have a permeability k that depends on ϵ according to

$$k(\epsilon) = K_\chi L^2 \epsilon^\chi\,, \tag{2}$$

where L is the length of a channel in the (monodisperse) foam, and K_χ is a dimensionless number. The characteristic exponent χ depends crucially on the boundary condition at the liquid/gas interface [9, 10].

One limiting case for the boundary conditions is assuming *rigid* interfaces [11, 12] causing Poiseuille-type flow in the channels. Because the nodes are small, the viscous drag in the channels dominates. The

permeability is proportional to r^2 and thus (via (1)) to ϵ, so that $\chi = 1$. The dimensionless prefactor of (2) has been determined numerically as $K_1 \approx 6.3 \times 10^{-3}$ [8, 13].

The other limiting case is that of *mobile* interfaces with no-stress boundary conditions, resulting in plug-like flow in the channels. The viscous dissipation is then dominated by the mixing and bending of flows in the nodes (node-dominated drainage, [4, 8]). As the nodes only cover a fraction $\sim r/L$ of the liquid volume, the effective permeability is proportional to rL, and thus to $\epsilon^{1/2}$, which gives $\chi = 1/2$. For one-dimensional forced drainage experiments in narrow tubes with Dawn™ dish detergent or SDS surfactant (sodium dodecyl sulfate) we found that a best fit yields $\chi \approx 0.6$, which agrees well with this node-dominated limit [4, 8]. Evaluating the dimensionless prefactor K_χ is very difficult; from extensive experiments in our laboratory it appears that its value is not entirely independent of L, as the geometry and interfacial rheology undergo changes with bubble size. For SDS-generated bubbles of the size used in the experiments presented below ($L \approx 0.085\,\mathrm{cm}$), the one-dimensional experiments yield $K_{0.6} \approx 4.2 \times 10^{-3}$ and $K_{1/2} \approx 3.0 \times 10^{-3}$, respectively.

In a one-dimensional drainage experiment, liquid is confined to a narrow geometry such as a tube, in which the liquid spreads quickly over the tube cross section, showing non-trivial liquid flow dynamics in one direction only (generally that of gravity). However, capillarity acts in all directions and is a major factor shaping the flow if the overall geometry of the experiment is less confined. Whenever liquid is poured onto a foam, e.g. when pouring beer, liquid can be observed flowing in all directions. At the liquid source the foam's liquid volume fraction is high, and away from the source capillary forces draw the liquid from the wet to the dry part of the foam, much like water being absorbed into a (dry) sponge.

Liquid flow through the channel-like network of permeability $k(\epsilon)$ is driven by gravity $\rho\mathbf{g} \approx 981\,\mathrm{g\,cm^{-2}s^{-2}}$ and gradient of the capillary pressure $\nabla(\gamma/r)$ where γ is the surface tension and r is the characteristic radius of curvature of the Plateau border. The latter can be calculated in terms of ϵ from (1). The liquid velocity through the network of channels and nodes then follows from Darcy's law,

$$\mathbf{u} = \frac{k(\epsilon)}{\mu}\left(\rho\mathbf{g} + \nabla\left(\frac{\gamma\delta_\epsilon^{1/2}}{L\epsilon^{1/2}}\right)\right), \tag{3}$$

where $\mu \approx 0.01\,\mathrm{g\,s^{-1}cm^{-1}}$ is the viscosity of the aqueous liquid in the foam and $\gamma \approx 30\,\mathrm{g\,cm^{-2}}$ for SDS surfactant solutions. The spatial and temporal dynamics of ϵ are determined from the continuity equation $\frac{\partial}{\partial t}\epsilon + \nabla\cdot(\epsilon\mathbf{u}) = 0$. This leads to a generalized *foam drainage equation*,

$$\mu\frac{\partial\epsilon}{\partial t} + K_\chi L^2\rho\mathbf{g}\cdot\nabla\epsilon^{\chi+1} - \frac{K_\chi L\gamma\delta_\epsilon^{1/2}}{2\chi+1}\nabla^2\epsilon^{\chi+1/2} = 0 \tag{4}$$

for arbitrary permeability exponent χ. Note that, even though the flow is inertia-free, the resulting PDE is nonlinear because of the coupling of liquid volume fraction and flow speed. In simple cases, analytical solutions of (4) such as solitary waves are known [4, 11, 14]. In both the channel-dominated and the node-dominated limits, scaling laws for macroscopic liquid motion can be obtained [8]. In general, however, an accurate description of drainage has to take into account terms originating from both channel and node dissipation, which transforms the scaling laws into mixed scaling. Often, this mixing can be described by a single effective exponent such as the experimentally obtained $\chi \approx 0.6$ in the above example. We will call this approximation the *hybrid model*.

After a brief description of the experimental setup and some typical results, we will proceed to investigate numerically and analytically the properties of the different limits of the theory for Eq. (4).

2 Experiment

The experimental setup is centered around a Hele-Shaw cell made of two plane parallel UV-transmitting Plexiglas plates, spaced $H = 2.54\,\mathrm{cm}$ apart, about 1 m tall and 65 cm wide, as shown in Fig. 1a. The foaming liquid contains 10 g/l of SDS in distilled water, which is well above the critical micelle concentration (CMC) [15]. Fluorescein salt (0.25 g/l) is added to the solution whose fluorescence under UV exposure is detected with a CCD camera. A continuous slow flow of N_2 gas is forced through an extra-coarse porous glass frit inside the soap solution, filling the Hele-Shaw cell with bubbles of mean edge length $L = 0.085\,\mathrm{cm}$ with an edge-length polydispersity of about 50%. This broad distribution of edge lengths is common even for simulated random foams with exactly uniform volume [16]. The gas flow

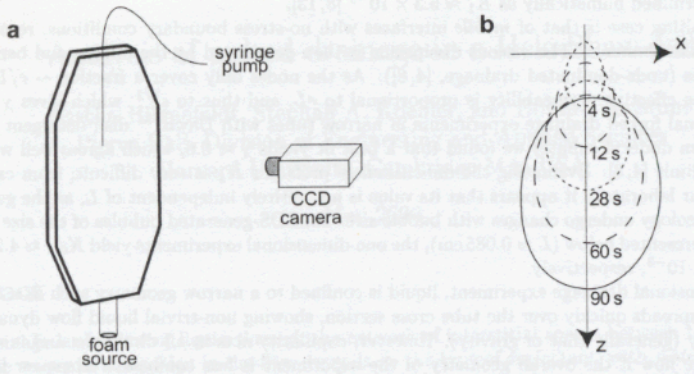

Figure 1: Schematic of Hele-Shaw cell with syringe pump and CCD camera (a). The Hele-Shaw cell has an octahedral shape to prevent stagnant zones as the foam flows from the bottom to the top. The syringe pump injects a prescribed volume of liquid into the foam-filled Hele-Shaw cell that is imaged by the camera. In (b) the lines of equal intensity (normalized to the peak intensity) of a 1.7 ml pulse in the plane of the Hele-Shaw cell is shown (injection is at $x = 0, z = 0$). Gravity pulls the pulse downwards and capillarity spreads the pulse radially.

continuously replenishes the foam, making it rise at a velocity of about 0.26 mm/sec. Thus, at a fixed position in space, the foam does not *coarsen* (cf. e.g. [17]); coarsening effects are also small over the height of the field of view of the camera.

The experiments presented here are for *pulsed drainage*, where a small volume (pulse) of the soap solution is injected near the center of the foam-filled cell. The point of injection sets the origin of the (x, z) coordinate system, with the x axis horizontal and the z axis pointing downwards. The time $t = 0$ is set by the end of the injection process.

This setup is designed to produce drainage data where ϵ is a function of the two coordinates x, z only. From (4) it is clear that the capillary spreading across the thickness of the Hele-Shaw cell (the y direction) occurs diffusively, with an effective diffusion constant

$$D = K_\chi L \gamma \delta_c^{1/2} \epsilon^{\chi - 1/2} / 2\mu \,. \tag{5}$$

With the parameters given above (assuming $\chi = 1/2$), we get $D \approx 0.16\,\mathrm{cm^2 s^{-1}}$. This means that the pulse spreads across the thickness H of the Hele-Shaw cell within ≈ 10 sec. Data taken at longer times should reflect genuine two-dimensional drainage.

In one-dimensional forced drainage experiments [4] we found that to a good approximation the fluorescence intensity is linearly proportional to ϵ, which we assume to be valid for the two-dimensional experiments here as well. The ratio of the pulse volume to the integrated total intensity was used to evaluate the prefactor of the proportionality for each individual run with an estimated error of about 20%. Figure 1b shows the fluorescence outlines (lines of equal relative intensity) of the spreading pulse at successive times. There is a strong similarity between this spreading phenomenon and the flow of a drop down an inclined plane [18].

3 A typical drainage pulse

Experimental data of 2-D pulsed drainage as well as more details on the setup have been published elsewhere [19]. A typical result can be seen in Fig. 2, in which the dynamics of a pulse with $V_{\mathrm{liq}} = 0.16$ ml are shown. In the $x-$direction ($z = 0$) the profiles spread out symmetrically, whereas in the $z-$direction ($x = 0$) the ϵ-profiles are biased downwards by the action of gravity. Thus, the peak of the pulse moves

downwards, while the entire profile broadens along both axes due to capillary forces. The dynamics of the peak can be characterized by its position $z_{\max}$ and liquid volume fraction $\epsilon_{\max}$.

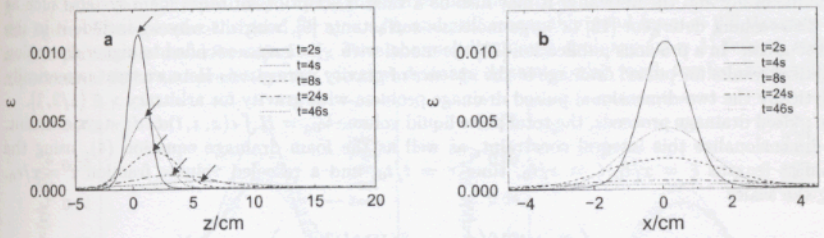

Figure 2: (a) Experimental data of the drainage of a $V_{\text{liq}} = 0.16\,\text{ml}$ pulse along the vertical $z-$axis at $x = 0$, and (b) along the horizontal x-axis at $z = 0$. The arrows in (a) indicate the location of the peak, $z_{\max}$, and the peak liquid volume fraction, $\epsilon_{\max}$.

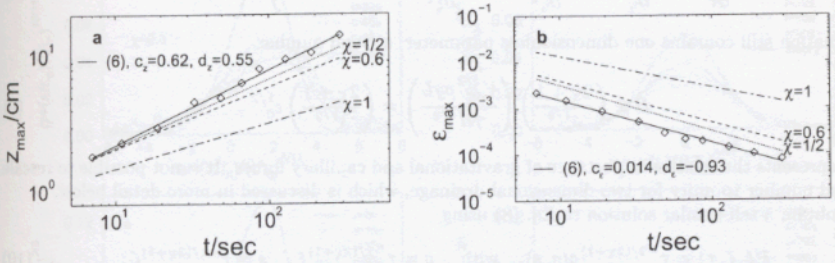

Figure 3: Dynamics of (a) the vertical position $z_{\max}$ and (b) the height $\epsilon_{\max}$ of the pulse maximum for $V_{\text{liq}} = 0.16$ ml bolus. Symbols show experimental values, with solid lines as best fits to Eq. (6). The other lines are small Bond number predictions (i.e., small pulse volumes) from models with different characteristic exponents χ, inferred from (15) and (16) or their analogs in [19]. There are no adjustable parameters in these theoretical curves. Of the various predictions, the dotted line for the node-dominated model ($\chi = 1/2$) seems to agree best with experiment, with the hybrid model ($\chi = 0.6$) relatively close and clear discrepancies arising for the channel-dominated approach ($\chi = 1$).

Figure 3 shows the dynamics of the pulse's peak and peak height for the same pulse. These quantities could be tracked for several hundred seconds using the fluorescence technique described above. On the log-log plot the points fall on straight lines suggesting power-law behavior of the form

$$z_{\max}/\text{cm} = c_z(t/\text{sec})^{d_z} \quad \text{and} \quad \epsilon_{\max} = c_\epsilon(t/\text{sec})^{d_\epsilon}\,. \tag{6}$$

For our example, the best fits yield $c_z \approx 0.62$, $d_z \approx 0.55$ and $c_\epsilon \approx 0.014$, $d_\epsilon \approx -0.93$. In fact, repeating the same experiment for pulse volumes V_{liq} ranging from 0.02 ml to 1.32 ml, similar power law behavior is found [19], with the prefactors c_z and c_ϵ increasing with liquid content. The exponents exhibit a slight scatter around mean values of $d_z \approx 0.6$ and $d_\epsilon \approx -0.9$.

4 Theory

As described above, for experiments with aqueous SDS foams the experimentally found characteristic exponent $\chi \approx 0.6$ is close to the node-dominated limit, making a description using $\chi = 1/2$ quite successful in reproducing experimental data, as reported in [19]. In the remainder of this paper, we will compare these results to the predictions of the channel-dominated model, as well as to the hybrid model

with $\chi = 0.6$. The theory is qualitatively different from the node-dominated case in several aspects, cf. also the work of Grundy [20]. Although the channel-dominated theory is found to be unable to reproduce results of experiments with aqueous SDS foams [4, 8, 21], it has received much attention in the literature both experimentally and theoretically. It may also be a valid description for other foam systems such as Fairy^{TM} dishwashing detergent [12] or large-molecule surfactants [9], which is why we include it in the present discussion. In a previous publication [22] the model with $\chi = 1$ was extended to higher dimension and analytical results for pulsed drainage in the *absence* of gravity were given. Here we treat numerically and analytically the two-dimensional pulsed drainage problem with gravity for arbitrary $\chi \in (1/2, 1]$.

While pulsed drainage proceeds, the total pulse liquid volume $V_{\mathrm{liq}} = H \int \epsilon(x, z, t) dx\, dz$ stays constant. We non-dimensionalize this integral constraint, as well as the foam drainage equation (4), using the dimensionless lengths $\xi = x/\ell_0, \zeta = z/\ell_0$, time $\tau = t/t_0$, and a rescaled volume fraction $\tilde{\epsilon} = \epsilon/\epsilon_0$. Choosing the scales

$$\ell_0 = \frac{\gamma}{\rho g L}\,,\quad t_0 = \left(\frac{2\chi+1}{K_\chi \delta_\epsilon^{1/2}}\right)\left(\frac{\mu \gamma^{2\chi} H^{\chi-1/2}}{(\rho g)^{2\chi+1} V_{\mathrm{liq}}^{\chi-1/2} L^{2\chi+2}}\right)\,,\quad \epsilon_0 = \frac{V_{\mathrm{liq}}}{H \ell_0^2}\,, \tag{7}$$

one obtains a dimensionless foam drainage equation for arbitrary characteristic exponent χ,

$$\frac{\partial \tilde{\epsilon}}{\partial \tau} + \mathcal{B}\frac{\partial \tilde{\epsilon}^{\chi+1}}{\partial \zeta} - \frac{\partial^2 \tilde{\epsilon}^{\chi+1/2}}{\partial \zeta^2} - \frac{\partial^2 \tilde{\epsilon}^{\chi+1/2}}{\partial \xi^2} = 0 \quad \text{with} \quad \int \tilde{\epsilon}\, d\xi\, d\zeta = 1\,. \tag{8}$$

This equation still contains one dimensionless parameter, a Bond number

$$\mathcal{B} \equiv \left(\frac{2\chi+1}{\delta_\epsilon^{1/2}}\right)\left(\frac{V_{\mathrm{liq}}^{1/2} \rho g L}{\gamma H^{1/2}}\right) = \left(\frac{2\chi+1}{\delta_\epsilon^{1/2}}\right)\epsilon_0^{1/2}\,, \tag{9}$$

which represents the relative importance of gravitational and capillary forces. It is not possible to rescale the Bond number to unity for two-dimensional drainage, which is discussed in more detail below.

We obtain a self-similar solution to Eq. (8) using

$$\tilde{\epsilon}(\xi, \zeta, \tau) = \tau^{-2/(2\chi+1)} g(q, s) \quad \text{with} \quad q = \tau^{-1/(2\chi+1)}\xi\,,\quad s = \tau^{-1/(2\chi+1)}\zeta\,; \tag{10}$$

a partial differential equation in similarity coordinates $(q,\ s)$ follows:

$$-\frac{1}{2\chi+1}\left(\frac{\partial (qg)}{\partial q} + \frac{\partial (sg)}{\partial s}\right) + \mathcal{B}\frac{\partial g^{\chi+1}}{\partial s} - \left(\frac{\partial^2 g^{\chi+1/2}}{\partial q^2} + \frac{\partial^2 g^{\chi+1/2}}{\partial s^2}\right) = 0\,. \tag{11}$$

This self-similar transformation will yield a PDE like (11) for any dimension d. However, only in two dimensions does the volume remain conserved, because $\int \tilde{\epsilon}(\xi, t)\, d^d\xi \propto t^{(2-d)/(2\chi+1)}$, with ξ being the vector of non-dimensional spatial coordinates in d dimensions. On the other hand, removing the constraint of conserved volume gives another freedom of rescaling which allows for $\mathcal{B}$ to be set to one when $d \neq 2$ (cf. the one-dimensional local similarity solutions in [8]).

4.1 Numerics

We use an operator-splitting code to obtain numerical solutions for both the foam drainage equation (8) and its self-similar version (11). These calculations assume a perfectly dry background foam into which the pulse is introduced, so that the boundary conditions are $\tilde{\epsilon} = g = 0$ far away from the pulse. In experiment, a certain background liquid volume fraction ϵ_b persists as the pulse is introduced. Moreover, ϵ_b is not uniform, but increases towards the bottom of the foam (stationary nonzero liquid profile, cf. e.g. [23]). The values of ϵ_b in the field of view of the camera (relatively high above the bottom of the foam) are very small ($\lesssim 10^{-4}$). Nevertheless, this can lead to an acceleration of the drainage dynamics for long times, as the pulse drains into the slightly wetter region of the foam. For most of the comparison between theory and experiment we describe, the influence of ϵ_b is small.

Simulations of (11) result in a stationary pulse profile in (g, q, s) space onto which the experimental data should collapse for long times. Figure 4 attempts to collapse the experimental measurements from Fig. 2 ($V_{\mathrm{liq}} = 0.16\,\mathrm{ml}$) in this fashion for various χ. Parts a,b of the figure show the vertical and horizontal

collapse for $\chi = 1/2$ (node-dominated model) as reported in [19]. In c,d, the results for the hybrid model ($\chi = 0.6$) are presented, while e,f show collapses for $\chi = 1$. Scaling exponents and coefficients are different for different χ, and so are the Bond numbers corresponding to $V_{\rm liq}$, namely $\mathcal{B} \approx 3.37, 3.71$, and 5.06 for $\chi = 1/2, 0.6$, and 1, respectively. With these $\mathcal{B}$ values, numerical simulations yield the heavy lines in the figure. The agreement is good for $\chi = 1/2$, and still reasonably good for $\chi = 0.6$ (considering that no free parameters could be adjusted). Pure channel-dominated drainage ($\chi = 1$) fails to collapse the experimental data, and predicts much too slow drainage dynamics with much too localized pulses.

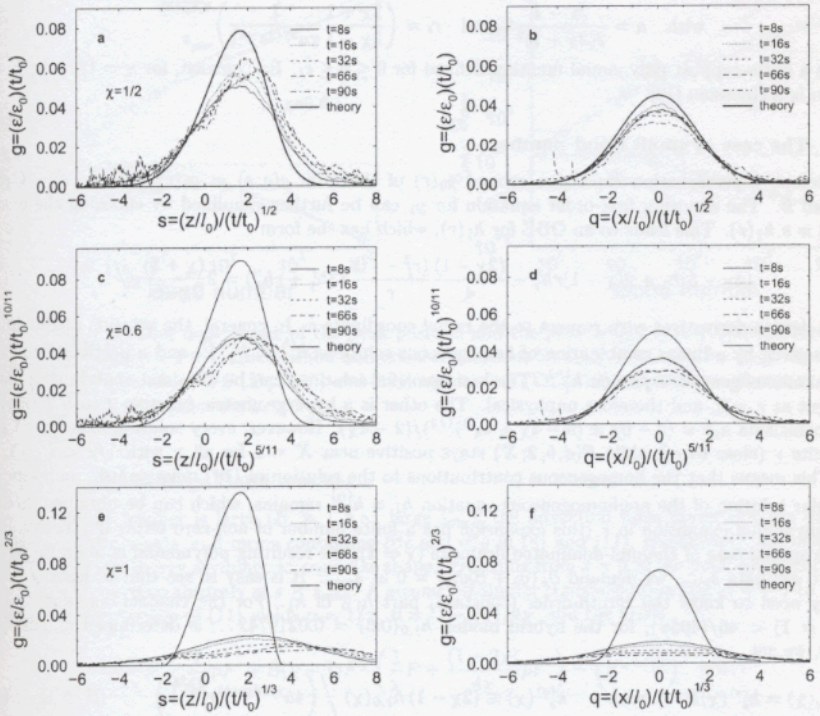

Figure 4: Collapse of the vertical and horizontal profiles from Fig. 2 when rescaled according to (10) for different characteristic exponents: $\chi = 1/2$ (a,b) from [19], $\chi = 0.6$ (c,d), and $\chi = 1$ (e,f). The pulse volume is $V_{\rm liq} = 0.16\,{\rm ml}$; corresponding computational results (PDE simulation of Eq. (11) with $\mathcal{B} = 3.37, 3.71$, and 5.06, respectively) are shown as heavy lines. The collapse is best for the node-dominated and poorest for the channel-dominated drainage model.

4.2 Analytical results

From the self-similar scaling (10), the predictions for the exponents d_z and d_ϵ in (6) are obviously $d_z = 1/(2\chi + 1)$ and $d_\epsilon = -2/(2\chi + 1)$. The measured values are consistent with the node-dominated limit $\chi = 1/2$ [19]. The hybrid exponent $\chi = 0.6$ [4,8] does slightly better in fitting d_ϵ. The anomalously high value of d_z is presumably due to the above-mentioned acceleration of drainage induced by the background volume fraction ϵ_b. Numerical simulations with $\epsilon_b \neq 0$ (not shown) support this conclusion.

Analytical computations can yield results for the prefactors c_z and c_ϵ as well, at least in certain limiting cases. For node-dominated ($\chi = 1/2$) drainage, these have been reported elsewhere [19]. We present results for the more general case $1/2 < \chi \leq 1$ here. The analytical treatment is slightly different from $\chi = 1/2$, mainly because the pulse has compact support for $\chi > 1/2$, but is of infinite extent for $\chi = 1/2$ [19].

4.2.1 Gravity-free case

Since capillarity is the only driving force for zero Bond number, the pulse will have rotational symmetry, so we introduce the radial coordinate $r = (q^2 + s^2)^{1/2}$. The analytical solution of (11) for $\mathcal{B} = 0$ and channel-dominated drainage ($\chi = 1$) was given in [22]. It is easily generalized for arbitrary χ to yield the solution

$$g_0(r) = \left[a\left(r_l^2 - r^2\right)\right]^{\frac{2}{2\chi-1}} \quad \text{for } 1/2 < \chi \leq 1\,, \tag{12}$$

$$\text{with} \quad a = \frac{2\chi - 1}{2(2\chi+1)^2} \quad \text{and} \quad r_l = \left(\frac{2\chi+1}{2\chi-1}\frac{1}{\pi a^{2/(2\chi-1)}}\right)^{\frac{2\chi-1}{2(2\chi+1)}}. \tag{13}$$

$g_0(r)$ is a finite-support polynomial function defined for $0 \leq r \leq r_l$. By contrast, for $\chi = 1/2$, the $\mathcal{B} = 0$ solution is a Gaussian [19].

4.2.2 The case of small Bond number

We attempt a perturbation expansion around $g_0(r)$ of the form $g(q,s) = g_0(r) + \mathcal{B}g_1(q,s) + \mathcal{O}(\mathcal{B}^2)$ for small $\mathcal{B}$. The resulting first-order equation for g_1 can be further simplified by choosing the ansatz $g_1(q,s) = s\, h_1(r)$. This leads to an ODE for $h_1(r)$, which has the form

$$(4\chi - 5)h_1 + 2(\chi-1)rh_1' - \frac{(2\chi-1)}{4}\frac{(r_l^2 - r^2)}{r}(3h_1' + rh_1'') = 2\frac{(\chi+1)}{2\chi+1}g_0^{3/2}. \tag{14}$$

Primes denote derivatives with respect to the radial coordinate r. In general, the solution of this linear ODE is given by a linear combination of homogeneous solutions $h_1^{(h,1)}$, $h_1^{(h,2)}$, and a particular solution of the nonhomogeneous equation $h_1^{(n)}$. The homogeneous solutions can be obtained analytically; one is divergent at $r = 0$, and therefore unphysical. The other is a hypergeometric function $F(a,b,2,(r/r_l)^2)$ with coefficients $a, b = (5 - 6\chi \pm (5 - 4\chi + 4\chi^2)^{1/2})/(2 - 4\chi)$. However, every solution must go to zero at a finite r (close to r_l) while $F(a,b,2;X)$ stays positive near $X = 1$ for all χ with $1/2 < \chi \leq 1$, cf. [24]. This means that the homogeneous contributions to the solution of (14) must vanish, and only the particular solution of the nonhomogeneous equation $h_1 = h_1^{(n)}$ remains, which can be obtained directly by a polynomial expansion in r (this expansion has a finite number of non-zero terms if χ is rational). For the special case of channel-dominated drainage ($\chi = 1$), the resulting polynomial is of 6th order. In order to evaluate $s_{\max}$, we demand $\partial_s\left(g_0 + \mathcal{B}sh_1\right) = 0$ at $s_{\max}$. It is easy to see that to leading order, we only need to know the zeroth-order (constant) part $h_{1,0}$ of h_1. For the channel-dominated limit, $h_{1,0}(\chi = 1) = 46/(495\pi)$; for the hybrid model, $h_{1,0}(0.6) = 0.0219742\ldots$ is determined numerically. Finally, we get

$$s_{\max}^{(s)}(\chi) = k_s^{(s)}(\chi)\mathcal{B} \qquad \text{with} \qquad k_s^{(s)}(\chi) \equiv (2\chi - 1)\, h_{1,0}(\chi) \Big/ \left(4a^{2/(2\chi-1)} r_l^{\frac{6-4\chi}{2\chi-1}}\right) \qquad (\mathcal{B} \ll 1)\,. \tag{15}$$

The superscript $^{(s)}$ indicates small Bond number. The special cases are $k_s^{(s)}(1) = 6^{1/3}23/(55\pi^{2/3}) = 0.354255\ldots$ and $k_s^{(s)}(0.6) = 0.455983\ldots$, respectively. The prefactors do not show much variation with χ, but $s_{\max}^{(s)}$ does become significantly different because $\mathcal{B}$ depends on χ as well (see (9)). In Fig. 5, we compare the results of this asymptotic formula for the location of the pulse maximum in rescaled coordinates to simulations of (11) for $\chi = 0.6$ and $\chi = 1$. The agreement between the analytical predictions and the numerical calculations is excellent even up to $\mathcal{B} \lesssim 10$, well beyond the naive small $\mathcal{B}$ regime. So far, experiments have been conducted for $1 \lesssim \mathcal{B} \lesssim 10$ [19], and were found to be well described by this limit when $\chi = 1/2$.

Due to the logarithmic scales of Fig. 5, it is hard to distinguish between the $\chi = 0.6$ and $\chi = 1$ predictions. For the experimental example given above ($V_{\text{liq}} = 0.16\,\text{ml}$), we therefore reconvert the values of (15) into physical variables and try to reproduce the dynamics $z_{\max}(t)$. In Fig. 3a we show these predictions for $\chi = 0.6$ and $\chi = 1$, and compare them to the earlier results of node-dominated ($\chi = 1/2$) calculations. The node-dominated model does best in reproducing the experiment, with the hybrid model a close second, and channel-dominated drainage in relatively poor agreement.

With the result $s_{\max}^{(s)} \propto \mathcal{B}$ for small $\mathcal{B}$, we see from the expansion above that the peak value does not vary to first order in $\mathcal{B}$,

$$g_{\max}^{(s)} = g_{0,\max} + \mathcal{O}(\mathcal{B}^2) = (ar_l^2)^{2/(2\chi-1)} + \mathcal{O}(\mathcal{B}^2) \qquad (\mathcal{B} \ll 1)\,. \tag{16}$$

The horizontal dashed lines in Fig. 5 represent this prediction for $\chi = 0.6, 1$, which coincides with the PDE solutions (circles). These theoretical values for $g^{(s)}_{\max}$, converted into the real-space variable $\epsilon_{\max}(t)$, are shown in Fig. 3b, together with the $\chi = 1/2$ result of [19]. Again, the node-dominated limit is closest to the measurements, and $\chi = 1$ shows the poorest agreement.

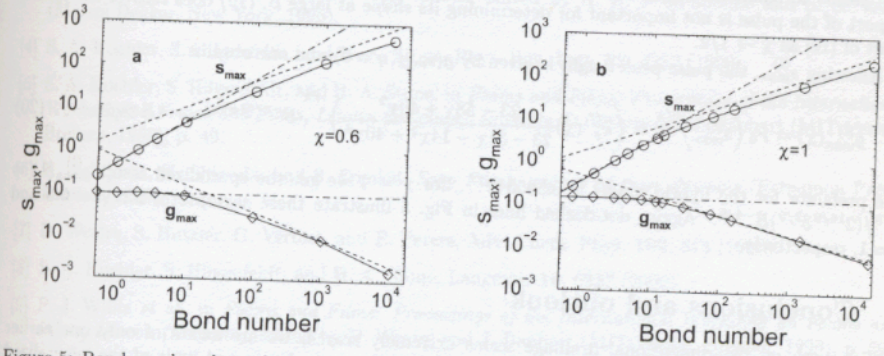

Figure 5: Bond number dependence of the peak position and the peak height in self-similar coordinates for $\chi = 0.6$ (a) and $\chi = 1$ (b). Circles show numerical simulations for $s_{\max}$, diamonds for $g_{\max}$. Analytical results for the limits of small $\mathcal{B}$ (Eq.s (15) and (16)) and large $\mathcal{B}$ (Eq.s (19) and (20)) are shown as dashed and dot-dashed lines, respectively.

4.2.3 The case of large Bond number

When the Bond number is large ($\mathcal{B} \gg 1$, i.e., large $V_{\rm liq}$), the advection term dominates the drainage process along the s-axis, and terms containing $\partial^2_\xi \bar{\epsilon}$ and $\partial^2_s g$ in (8) and (11), respectively, are negligible. The pulse takes on a very asymmetric, cone-like shape, stretching from $s = 0$ to the peak coordinate $s_{\max}$, with g dropping to zero abruptly at $s \gtrsim s_{\max}$. A *second* self-similar transformation $g(q, s) = s^\alpha F(p \equiv s^\beta q)$ in the truncated version of (11) yields $\alpha = 1/\chi$, $\beta = (1 - 2\chi)/4\chi$, and the ODE

$$-\frac{1}{\chi}F - \frac{1}{4\chi}pF' + \mathcal{B}(\chi+1)F^\chi\left(\frac{1}{\chi}F + \frac{(1-2\chi)}{4\chi}pF'\right) - \left(F^{\chi+1/2}\right)'' = 0\,. \tag{17}$$

Because of axial symmetry in q, $F(p)$ must be an even function. As the pulses are long and slender for large $\mathcal{B}$, they cover mostly small values of p. Therefore, we can expand $F(p) \approx F_0 + F_2 p^2 + F_4 p^4 + \mathcal{O}(p^6)$. Solving for the leading-order coefficients of the expansion in p^2, one obtains lengthy analytical expressions for F_0, F_2, and F_4. To calculate the coordinate $s_{\max}$ of the pulse maximum (which also gives an approximation to the finite length of the pulse along s), we use the condition of volume conservation, namely

$$1 \approx \int_0^{s_{\max}} \int_{-p_0(s)}^{+p_0(s)} g(q,s)\, dp\, ds\,, \tag{18}$$

with $\pm p_0(s)$ fulfilling $g(\pm p_0(s), s) = 0$. We eventually find for $1/2 < \chi < 1$:

$$s^{(l)}_{\max}(\chi) = k^{(l)}_s(\chi)\mathcal{B}^{\frac{3+2\chi}{3+6\chi}} \quad \text{for} \quad \mathcal{B} \gg 1\,, \quad \text{where}$$

$$k^{(l)}_s(\chi) \equiv \left[\frac{45}{8}\left(\frac{2\chi+1}{\sqrt{3-2\chi}-1}\right)^{1/2}\frac{(1-\chi)}{\chi}\frac{(1-\chi^2)^{1/2}}{(7-6\chi-\sqrt{3-2\chi})}\frac{\left(23-31\chi-14\chi^2+40\chi^3\right)^{3/4\chi}}{(23-58\chi+40\chi^2)^{1/2+3/4\chi}}\right]^{\frac{4\chi}{3+6\chi}}, \tag{19}$$

and $^{(l)}$ indicates large Bond number. For the hybrid model, we find the prefactor $k^{(l)}_s$ (as defined above) to be $k^{(l)}_s(0.6) = 2.25412\ldots$. This asymptote is indicated as the dot-dashed line in Fig. 5a, which is in

good agreement with the simulations for large $\mathcal{B}$ (circles)[1]. The maximum experimental injection volumes ($\mathcal{B} \lesssim 10$) are too small to reach this scaling regime. Note that for $\chi = 1$ the fourth-order solution (19) is singular, but the singularity is removable, so that we get $k_s^{(l)}(1) = 3^{16/9}/(2^{7/9}5^{5/9}) = 1.68176\ldots$. This result is shown as dot-dashed line in Fig. 5b for channel-dominated theory. The singular character of this limit seems to result in some loss of accuracy, but the agreement is still very good. Because the finite support of the pulse is not important for determining its shape at large $\mathcal{B}$, (19) does recover the special result of [19] as $\chi \to 1/2$.

Knowing $s_{\max}^{(l)}$, the pulse peak height is given by $g(s_{\max}, q = 0)$ and one obtains

$$g_{\max}^{(l)}(\chi) = F_0 \left(s_{\max}^{(l)}\right)^{1/\chi} = \left(k_s^{(l)}(\chi)\frac{23 - 58\chi + 40\chi^2}{23 - 31\chi - 14\chi^2 + 40\chi^3}\right)^{1/\chi} \mathcal{B}^{-4/(3+6\chi)} \qquad (\mathcal{B} \gg 1). \qquad (20)$$

The prefactor for the hybrid model is $0.595342\ldots$, for $\chi = 1$ we get the specialized result $g_{\max}^{(l)}(1) = 5^{4/9}/(2^{16/9}3^{2/9})\mathcal{B}^{-4/9}$. Again, dot-dashed lines in Fig. 5 illustrate these asymptotes for $\chi = 0.6$ and $\chi = 1$, respectively.

5 Conclusions and outlook

Earlier work on two-dimensional drainage seems extremely scarce; we are aware of only one earlier numerical study [25]. Elsewhere [19] we have shown that the node-dominated limit of the generalized foam drainage equation is quite successful in describing the dynamics of two-dimensional pulsed drainage. The present work compares these results to the other (channel-dominated) limit and to the predictions of a hybrid model interpolating between the two extremes. As expected, the channel-dominated predictions are quite different from the experimental data obtained in our laboratory, while a hybrid model close to the node-dominated limit does well in fitting the measurements. We find, however, that a relatively small deviation of χ from the node-dominated limit $\chi = 1/2$ can induce noticeable changes in the predicted shape of the drainage pulses (see Fig. 4). We are planning experiments with the protein surfactant bovine serum albumin (BSA) to further investigate the channel-dominated limit.

In the theory of 2-D pulsed drainage one dimensionless group – the Bond number – is crucial for the motion and shape of the pulses. We have varied it over one decade changing the amount of liquid in the pulse. Characteristic power laws determine the dynamics of the pulse maximum coordinate and height. In the asymptotic cases of small and large Bond numbers, we have presented detailed analytical predictions for both the exponents and the prefactors of these power laws for arbitrary hybrid models as well as for the channel-dominated limit. Mathematically, these calculations are different from the node-dominated limit because the solutions for $\chi = 1/2$ have infinite extent (the gravity-free solution is a Gaussian [19]), whereas all solutions for $1/2 < \chi \leq 1$ have compact support (polynomials for $\mathcal{B} = 0$). Often, however, the general case presented here incorporates $\chi \to 1/2$ as a well-defined limit.

With analytical predictions available for the whole range of characteristic exponents between the channel-dominated model (indicative of rigid interfaces) and the node-dominated model (indicative of mobile interfaces), it is possible to make a comparison with experiments in which the mobility of the interface can be varied continuously. Durand et al. [10] have done such an experiment for 1-D forced drainage, varying the amount of dodecanol added to the SDS solution.

In various applications, two- or three-dimensional drainage is important, e.g. in the textile industry, food processing, or oil recovery. The generalization of the present analysis to three dimensions is straightforward. Data in 3-D can be acquired using MRI [26, 27] or X-ray scattering (CAT scan) techniques. The latter would allow for faster scanning of the drainage process. Recently foams in micro-gravity environments, such as the impending space station, have been investigated [28], allowing for an experimental realization of the $\mathcal{B} = 0$ limit of the present theory, in which drainage is solely due to capillarity.

Acknowledgments: We thank A. G. Evans for his guidance and support through the MURI project on Ultralight Metal Structures, A. Kraynik for numerous helpful discussions, and M. Brenner who wrote the original version of the PDE solver.

[1] Relaxation simulations of (11) converge only slowly for large $\mathcal{B}$ and are computationally expensive because of the strong pulse asymmetry, so that the values of $s_{\max}, g_{\max}$ for $\mathcal{B} \geq 1000$ are somewhat uncertain.

References

[1] J. J. Bikerman, *Foams* (Springer, New York, 1973).

[2] C. Isenberg, *The Science of Soap Films and Soap Bubbles* (Dover, London, 1992).

[3] *Foams, Theory, Measurements and Applications*, edited by R. K. Prud'homme and S. A. Khan (Marcel Dekker, New York, 1996).

[4] S. A. Koehler, S. Hilgenfeldt, and H. A. Stone, Phys. Rev. Lett. **82**, 4232 (1999).

[5] S. A. Koehler, S. Hilgenfeldt, and H. A. Stone, in *Foams and Films: Proceedings of the International Workshop on Foams and Films, Leuven (Belgium)*, edited by D. Weaire and J. Banhart (MIT-Verlag, Bremen, 1999), p. 49.

[6] K. J. Mysels, K. Shinoda, and S. Frankel, *Soap Films, studies of their thinning* (Pergamon Press, London, 1959).

[7] D. Weaire, S. Hutzler, G. Verbist, and E. Peters, Adv. Chem. Phys. **102**, 315 (1997).

[8] S. A. Koehler, S. Hilgenfeldt, and H. A. Stone, Langmuir **16**, 6327 (2000).

[9] P. J. Wilde *et al.*, in *Foams and Films: Proceedings of the International Workshop on Foams and Films, Leuven (Belgium)*, edited by D. Weaire and J. Banhart (MIT-Verlag, Bremen, 1999), p. 59.

[10] M. Durand, G. Martinoty, and D. Langevin, Phys. Rev. E **60**, R6307 (1999).

[11] I. I. Gol'dfarb, K. B. Kann, and I. R. Shreiber, Fluid Dynamics **23**, 244 (1988).

[12] G. Verbist, D. Weaire, and A. Kraynik, J. Phys. Condens. Matter **8**, 3715 (1996).

[13] R. A. Leonard and R. Lemlich, A.I.Ch.E. Journal **11**, 18 (1965).

[14] G. Verbist and D. Weaire, Europhys. Lett. **26**, 631 (1994).

[15] R. K. Prud'homme and G. G. Warr, in *Foams*, edited by R. K. Prud'homme and S. A. Khan (Marcel Dekker, New York, 1996), pp. 511–553.

[16] A. Kraynik, 2000, private communication.

[17] D. J. Durian, D. A. Weitz, and D. J. Pine, Phys. Rev. A **44**, R7902 (1991).

[18] F. J. Higuera, Phys. Fluids **7**, 2918 (1995).

[19] S. A. Koehler, S. Hilgenfeldt, and H. A. Stone, Europhys. Lett. in submission (2000).

[20] R. E. Grundy, IMA J. of Appl. Math. **31**, 121 (1983).

[21] D. Desai and R. Kumar, Chem. Eng. Sci. **37**, 1361 (1982).

[22] S. A. Koehler, H. A. Stone, M. P. Brenner, and J. Eggers, Phys. Rev. E **58**, 2097 (1998).

[23] G. Narsimhan and E. Ruckenstein, in *Foams: Theory, Measurements and Applications*, edited by R. K. Prud'homme and S. A. Khan (Marcel Dekker, New York, 1996), pp. 99–187.

[24] M. Abramowitz and I. A. Stegun, *Handbook of Mathematical Functions* (Dover, New York, 1972).

[25] S. Neethling and J. J. Cilliers, in *Foams and Films: Proceedings of the International Workshop on Foams and Films, Leuven (Belgium)*, edited by D. Weaire and J. Banhart (MIT-Verlag, Bremen, 1999), pp. 117–124.

[26] M. J. McCarthy, AIChE J. **36**, 287 (1990).

[27] C. P. Gonatas *et al.*, Phys. Rev. Lett. **75**, 573 (1995).

[28] B. Kronberg, L.-M. Trejo, M. Adler, and P. Holm, in *Foams and Films: Proceedings of the International Workshop on Foams and Films, Leuven (Belgium)*, edited by D. Weaire and J. Banhart (MIT-Verlag, Bremen, 1999), pp. 9–16.